JGR Space Physics

RESEARCH ARTICLE
10.1029/2021JA029690

Modeling of Possible Plume Mechanisms on Europa

Audrey Vorburger[1,2] **and Peter Wurz**[1]

[1]Physikalisches Institut, University of Bern, Bern, Switzerland, [2]Department of Physics, Umeå University, Umeå, Sweden

Key Points:

- Roth observations agree well with plume modeling (200 km height, 1.5e16 cm^{-2} column densities, two distinct plumes ~500 km apart)
- No difference in Ly-α and OI 130.4 nm emission profiles of three different plume → source cannot be determined from available observations
- Higher resolution images and mass spectrometer measurements would allow dis-tinction; prepare for data becoming available

Correspondence to:
A. Vorburger,
vorburger@space.unibe.ch

Citation:
Vorburger, A., & Wurz, P. (2021). Modeling of possible plume mechanisms on Europa. *Journal of Geophysical Research: Space Physics*, *126*, e2021JA029690. https://doi.org/10.1029/2021JA029690

Received 17 JUN 2021
Accepted 9 AUG 2021
Corrected 28 OCT 2021

This article was corrected on 28 OCT 2021. See the end of the full text for details.

Abstract Plumes spewing water high above Europa's surface have been inferred from several observation campaigns in the past decade. Whereas the occasional existence of plumes on Europa has thus been confirmed, the origin of the plumes remains uncertain. Most notably, it is still unclear whether the inferred plumes are of oceanic origin, possibly containing information about the ocean's habitability, or if they are of surficial nature, offering information on the highly processed surface instead. In this study, we use a Monte-Carlo model to analyze three different plume models, two of which are surficial (near-surface liquid inclusion and diapir), and one of which originates in the sub-surface ocean (oceanic plume). We analyze all relevant Lyman-α and OI 1304 $\AA$ emission mechanisms to determine the three models' emission profiles. These profiles are then compared to the Hubble Space Telescope/Space Telescope Imaging Spectograph measurements presented by Roth, Saur, et al. (2014, https://doi.org/10.1126/science.1247051) with the goal of determining which ab initio model fits these measurements best. Our analyses show that all three models investigated produce similar Lyman-α and OI 130.4 nm emission profiles, with differences being perceivable only on scales well below the HST resolution and sensitivity. Since none of the models contradict the Roth, Saur, et al. (2014, https://doi.org/10.1126/science.1247051) observations, none of them can be ruled out as being the acting force behind the observed plumes. The currently available optical measurements are thus not sufficient to determine the physical nature of Europa's plumes, identification of which can only be achieved through higher resolution images or in situ measurements.

Plain Language Summary In this study, we model three different Europa plume types using a Monte-Carlo model. Two of the analyzed plume types have their origin in the near-surface layer (near-surface liquid inclusion and diapir), whereas one model originates in the sub-surface ocean (oceanic plume). To compare our model results to Hubble Space Telescope observations, we compute for each plume type the Lyman-alpha and OI 130.4 nm emission profile. Our analysis shows that all three plume types fit the plumes observed by the Hubble Space Telescope equally well. It is thus impossible to distinguish from the Hubble Space Telescope observations what the origin of the observed plumes is. To do so, images with higher resolution, or in situ measurements are required.

1. Introduction

Existence of liquid water under the icy crust on Europa was postulated over 40 years ago (see e.g., Cassen et al., 1979; Ojakangas & Stevenson, 1989; Reynolds et al., 1983; Squyres et al., 1983), and confirmed to be very likely through the observation of morphological evidence (e.g., domes, chaos areas, bands, and ridges) and through Galileo magnetometer measurements of an induced magnetic field (indicating an electrically highly conductive global layer near the surface, most probably salt water) shortly before the year 2000 (Carr et al., 1998; Khurana et al., 1998; Kivelson et al., 2000; Pappalardo et al., 1999).

This ocean is likely in direct contact with a silicate seafloor, enabling catalytic reactions and offering a wide array of chemical elements that can be dissolved in the oceanic water. The Near Infrared Mapping Spectrometer (NIMS) onboard Galileo detected non-ice material on Europa's surface, for which ocean-originating hydrated salt minerals, hydrated sulfuric acid, and hydrogen peroxide represent likely candidates (Brown & Hand, 2013; R. Carlson et al., 1996; R. W. Carlson et al., 1999, 2005; Dalton, 2007; Dalton et al., 2005; Granahan et al., 1997; Hanley et al., 2014; Loeffler & Baragiola, 2005; McCord et al., 1998, 1999; Pappalardo, 2010; Zolotov & Kargel, 2009). Plumes, if fed by the sub-surface ocean, provide unique means of analyzing said

ocean water hundreds of kilometers above Europa's surface, that is, without actually having to probe the ocean itself.

Offering such a high potential, plume observations were attempted early on. In the early 1980s, one Voyager 2 image showed potential in capturing a plume by containing two anomalously bright features on the southern hemisphere (e.g., Cook et al., 1982a, 1982b; Helfenstein & Cook, 1984; Squyres et al., 1983). These features were subsequently shown to be image artifacts and to not capture plume activity, though (see e.g., Phillips et al., 2000). Subsequently, also Galileo and HST images were analyzed in search for evidence of plume activity (e.g., Fagents, 2003; Phillips et al., 2000; Saur et al., 2011). No such evidence could be found in either, though.

The existence of plumes on Europa was only confirmed in 2014, when Roth, Saur, et al. (2014) reported on three HST/STIS observations that showed statistically significant coincident hydrogen Lyman-α and oxygen OI 130.4 nm surpluses indicative of plume activity above Europa's south pole. After this first positive plume detection, eight more sets of HST images were analyzed in search for plume evidence, but no pronounced or co-incident Lyman-α and OI 130.4 nm emission surpluses could be found in any of them (Roth, Retherford, et al., 2014; Roth et al., 2017). In 2016 and 2017, Sparks et al. (2016, 2017) reported on off-limb absorption features reminiscent of plume activity. These results were later refuted by Giono et al. (2020), though, who stated that the plume candidate features presented by Sparks et al. (2016) could also be explained by purely statistical fluctuations, with misalignment possibly falsely increasing the significance. Overall, based on their assessment, the Sparks et al. (2016) observations did thus not provide definite evidence for plume activity. Finally, in 2019, Paganini et al. (2019) reported on 17 Keck Observatory observations of Europa's atmosphere, which targeted water lines in the infrared spectral region near $\sim$2.9 μm and $\sim$5.5 μm. Out of the 17 observations, 16 dates indicated no detection of atmospheric emission features within sensitivity limits. One measurement, however, did contain evidence for a water vapor plume, active above Europa's leading hemisphere.

Possible evidence for Europa plume existence was also provided by plasma data from the Galileo spacecraft recorded during the E12 and the E26 flybys (Arnold et al., 2019; Blöcker et al., 2016; Huybrighs et al., 2020; Jia et al., 2018; though the Huybrighs et al., 2020 observations were very recently refuted by Jia et al., 2021). The data of both passes contain small, short-timed (on the order of a few minutes) perturbations in the measured magnetic field data and plasma wave spectra that are best reproduced by models where Europa's magnetospheric plasma interacts with local plumes.

The record of Europa plume observation attempts thus shows that plumes are hard to capture, especially given the fact that they seem to be sporadic phenomena. In addition, the individual plume studies do not lead up to one consistent picture of one and the same plume, but are rather a collection of standalone studies, each with its own independent plume.

Overall, it remains unclear whether the observed plumes originate in the sub-surface ocean or rather in the surface ice layer itself. Several release mechanisms can lead to plume emission from icy bodies, most of which are not linked to the sub-surface ocean, and do thus not provide information on the sub-surface ocean. Such release mechanisms include diapirs that transport thermal energy to the surface resulting in surface ice sublimation, near-surface liquid inclusions that immediately volatilize once exposed to space, and meteorite impacts that excavate surface ice material. In this paper we analyze different plume models and their respective Lyman-α and OI 130.4 nm emission profiles, to check which models seem likely candidate sources for the plume observed by Roth, Saur, et al. (2014).

The 2014 HST/STIS plume detections, which represent the plume observations against which we check our model results, are presented in detail in Section 2. In Section 3 we present three different plume models that originate either in the icy surface or in the sub-surface ocean, all of which are based on passive processes (i.e., with no energy introduced into the system). The implementation of said models into our Monte-Carlo code is described in Section 4, whereas the simulation results (including the resulting emission profiles) are presented in Section 5 and discussed in Section 6. We conclude the paper by reviewing the key findings of our analysis in Section 7, where we also set this work into a broader context and provide an outlook for future work.

Table 1
Observational, Measured, and Inferred Europa Plume Parameters as Presented by Roth, Saur, et al. (2014)

Observational parameters		
Sub-observer west longitude	79°–108°	
System III longitude	0°–218°	
Magnetic latitude range	–9–9°	
Europa true anomaly angle	185–218°	(Close to apocenter)
Duration	7 h	(Five consecutive images)
Resolution	71.5–74.9 km	
Measured parameters		
Radial expansion	200 ± 100 km	
Latitudinal expansion	~ 20°	(~545 km)
Uncertainty	1–2 pixels	(~100 km)
Position	~ 180°W/65°S	(Anti-Jovian meridian)
Plume Lyman-α brightness	420 ± 136 R and 604 ± 140 R	(Bins 12 and 13)
Plume OI 130.4 nm brightness	35 ± 17 R and 59 ± 18 R	(Bins 12 and 13)
Global Lyman-α brightness	46 R	(Without bins 12 and 13)
Global OI 130.4 nm brightness	16 R	(Without bins 12 and 13)
Inferred parameters		
Transverse column density	$1.5 \cdot 10^{16}$ cm^{-2}	
Surface density	(1.3 and 2.2) $\cdot 10^{9}$ cm^{-3}	(Bins 12 and 13)
H_2O particle content	(4.9 and 8.2) $\cdot 10^{31}$ molecules	(Bins 12 and 13)
H_2O mass content	~1,465 and 2,450 kg	(Bins 12 and 13)
Upward mass flux	~7,000 kg/s	
Upward velocity	~700 m/s	

Note. For emission brightness, surface density, and water content two values are given. These values correspond to the two plume sources modeled by Roth, Saur, et al. (2014) in their two source plume model.

2. December 2012 HST/STIS Plume Observations

In this section, we present the December 2012 HST/STIS plume observations in detail, including all relevant plume and observation (instrumentation) parameters (see Table 1). Both parameter types are used in Sections 5 and 6 to evaluate our model results, with the goal of identifying possible plume origins for the observed December 2012 plume. We chose to use this plume observation for comparison as it presents the most "direct" observation available, and presents the best defined characteristics.

On December 30, 2012, HST/STIS measured statistically significant coincident surpluses of hydrogen Lyman-α and oxygen OI 130.4 nm emission, observable over the same area near Europa's south pole for over ~7 h (Roth, Saur, et al., 2014). During the observation, Europa was close to its apocenter, moving from 189° to 218° in its orbit. The Lyman-α and oxygen OI 130.4 nm surpluses identified in the angular bins 12 and 13 each exhibit a radial spatial extension of 200 km and a latitudinal expansion of ~ 20° (~545 km). The authors state that interpretation of the derived scale height and radial profile (both determined phenomenologically) requires caution, though, because of the systematic uncertainties of the disk location by 1–2 pixels (i.e., ~100 km).

Using measured cross sections for electron-impact dissociative excitation and the standard plasma parameters for Europa (an electron density of 40 cm^{-3}, a dominant thermal electron population with a temperature of T_e = 20 eV, and a supra-thermal population with T_e = 250 eV and a 2% mixing ratio), Roth, Saur, et al. (2014) derived for the two H_2O plumes identified in the images transverse column densities on the order of ~ $1.5 \cdot 10^{16}$ cm^{-2}. The measurements are best fit by two local plume sources at longitudes/latitudes

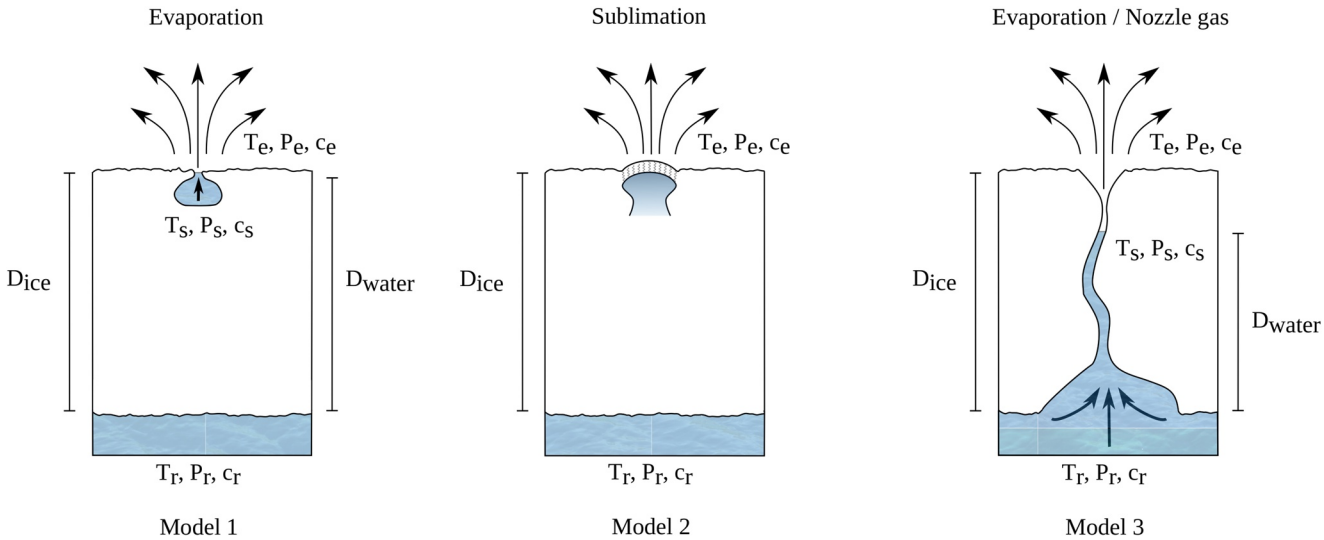

Figure 1. The three plume models taken into consideration: Model 1 = near-surface liquid inclusion, model 2 = diapir, and model 3 = ocean plume. Note that these cartoons are not shown to scale.

of 180°W/55°S and 180°W/75°S, respectively, each with a latitudinal expansion of 10° (or ~270 km on the surface), and with surface densities equal to $1.3 \cdot 10^9$ cm^{-3} and $2.2 \cdot 10^9$ cm^{-3}, respectively. The longitude of 180°W was chosen arbitrarily, since the surface source longitude location cannot be determined from the images. The derived water content amounts to $4.9 \cdot 10^{31}$ and $8.2 \cdot 10^{31}$ H_2O molecules (~1,465 kg and ~2,450 kg) for the two plumes, respectively. The authors also fit the plume with a single source located at 180°W/75°S, with the same scale height but a larger latitudinal extension of 20°. The single source plume model also fits the observations agreeably well, but not quite as well as the two source plume model.

3. Plume Physics

The geophysics that govern the observed plumes on Europa are still not well understood. Accordingly, different plume models have been proposed in the literature. These models differ in (a) the reservoir state (frozen or liquid), (b) the reservoir location (in the ice surface layer or in the sub-surface global ocean) and (c) the way particles are released from the reservoir (directly or in a modified manner). In the following we present three passive plume models, that is, models where no energy is being added to the system, schematic diagrams of which are presented in Figure 1.

3.1. Model 1: Near-Surface Liquid Inclusions

Liquid inclusions can exist close to Europa's surface in form of transient pockets of liquid water (see e.g., Fagents, 2003; Gaidos & Nimmo, 2000), usually formed through heating from below. The temperature (T_s), pressure (P_s), and sound speed (c_s) of the supply region (i.e., liquid inclusion) are completely decoupled from the sub-surface ocean reservoir (T_r, P_r, c_r). If such a liquid inclusion is exposed to space, it will experience immediate evaporation, due to the H_2O vapor pressure exceeding the ambient pressure (which is essentially vacuum, see e.g., Fagents, 2003). A near-surface liquid water inclusion will most likely resemble the ice crust in chemical composition and exhibit a temperature close to the triple point temperature (273.16 K), though this temperature might be slightly lower if the water contains additives that act as anti-freeze agents. The temperature, pressure, and sound speed of the ejecta (T_e, P_e, c_e) are governed directly by the supply region's vapor pressure.

Based on observations, plumes appear to be rare on Europa, a fact agreeing well with this model, as transient water pockets would only be exposed if a crack in the ice shell reached their exact location (Rhoden et al., 2015), an occurrence which is expected to happen only rarely. In addition, plumes formed from liquid

inclusions would be short-lived (existing only as long as the pocket has not been emptied out), another fact that agrees well with the Europa plume observations.

3.2. Model 2: Diapirs

Diapirs refer to thermally buoyant warm patches of ice that rise through the ice layer until either (a) the overlying ice is too cold and rigid to allow further movement, (b) the level of neutral buoyancy is reached, or (c) the diapir breaches the surface (see e.g., Fagents, 2003; Fagents et al., 2000; Rathbun et al., 1998; Quick & Marsh, 2016). If the surface is breached and warm ice is exposed to space, it immediately starts to sublimate, due to the sublimation pressure exceeding the ambient pressure, that is, vacuum. Diapir temperatures can range anywhere from >86 K (the minimum surface ice temperature) to <273.16 K (the water triple point, i.e., the temperature at which ice melts). In literature, values on the order of 210–270 K are usually proposed for Europa diapirs, with 250 K being the temperature considered most frequently (see e.g., Nimmo & Giese, 2005; Nimmo & Manga, 2002; Quick & Marsh, 2016; Rathbun et al., 1998). Again, the temperature, pressure, and sound speed of the ejecta (T_e, P_e, c_e) are governed directly by the surface ice's vapor pressure and are completely decoupled from the sub-surface ocean reservoir (T_r, P_r, c_r).

Based on morphological evidence, initial diapir radii are expected to be on the order of 2–4 km (Nimmo & Manga, 2002), and diapirs are expected to originate from within the top ~10 km of the ice layer (Rathbun et al., 1998). The chemical composition of the diapir resembles the chemical composition of the ice crust in most models, though it could also resemble the chemical composition of the water ocean if the diapir originates from the base of the ice surface layer (see Quick & Marsh, 2016 and references therein).

3.3. Model 3: Oceanic Plumes

From time to time, narrow fractures (tabular dikes or pipe-like conduits) might form in Europa's ice shell, either due to crustal or due to tidal stresses (exerted by Jupiter and the other Galilean satellites). If such a fracture is able to reach to the depth of the global ocean (D_{ice}), water will stream upwards in the suddenly opened crack due to the hydrodynamic pressure of the overlying ice shell. The hydrodynamic pressure of the ice shell depends on the ice shell thickness, the density of the ice, and Europa's gravitational acceleration. As the water column rises, it reaches the equilibrium height of $D_{\text{water}} = D_{\text{ice}} \cdot \rho_{\text{ice}}/\rho_{\text{water}}$, where it relaxes and from where it evaporates into space as long as the conduit above it remains open. In this model, the supply region's parameters (T_s, P_s, c_s) are directly linked to the oceanic reservoir parameters (T_r, P_r, c_r). Depending on the fracture's geometry, the water ejection into space might be either evaporation driven (e.g., with T_e, P_e, and c_e governed by the vapor pressure as in the previous models), or it might resemble a de Laval nozzle (i.e., a nozzle that gets narrower and then wider, accelerating the gas passing through it via isentropic expansion to the point where T_e, P_e, and c_e become jet-like [Clarke & Carswell, 2007]). In the latter case, the water flow is subsonic (Mach number <1) in the converging section of the conduit, sonic (Mach number = 1) at the throat (the fracture's narrowest part), and may become supersonic in the diverging section of the conduit (Mach number >1). The final Mach number at the vent is determined by the diameter ratio of the throat and the vent, which governs the subsequent expansion behavior (Anderson, 2003; Berg et al., 2016).

For Enceladus, Schmidt et al. (2008) inferred plausible conduit widths ranging from 10 cm to 1 m. At Europa, the conduits are expected to be somewhat broader, with Wilson et al. (1997) and Fagents (2003) proposing conduit widths in the range 1–30 m and 1–100 m, respectively. The liquid material released by oceanic plumes should match the water ocean composition, and might include aqueous solutions, vapor-rich sprays, or icy slurries (see also Fagents, 2003 and references therein). See Fagents et al. (2000); Thomson and Delaney (2001); Fagents (2003); Schmidt et al. (2008); Nimmo and Manga (2009); Yeoh et al. (2015); Quick and Marsh (2016); Yeoh et al. (2017) for further information on oceanic plumes and related activities on icy planetary bodies.

Table 2
Plume Model Parameters: $T_e je$ = Temperature of the Ejection Region, v_{tot} = Total Ejection Velocity, v_{rad} = Radial Ejection Velocity, v_{tan} = Tangential Ejection Velocity, α_{eje} = Ejection Angle, J_{eje} = Flux of Ejected Water Molecules, A_{res} = Reservoir Open Area

Model number	1	2			3	
Model type	Liquid	Diapir			Thermal	Jet
T_{eje} [K]	273.16	150	210	250	270	270
v_{tot} [ms^{-1}]	567	420	497	542	507	1,099
v_{rad} [ms^{-1}]	445	330	390	426	496	1,073
v_{tan} [ms^{-1}]	283	210	248	271	87	189
α_{eje} [deg]	58	58	58	58	80	80
J_{eje} [cm^{-2}s^{-1}]	9.19e21	1.24e14	1.20e19	1.19e21	7.11e21	7.11e21
A_{res} [m^2]	300	3e10	3e5	3,000	380	380

4. Monte-Carlo Model

The Monte-Carlo model used herein was originally developed to simulate Mercury's exosphere (Wurz & Lammer, 2003). It has since been continuously upgraded and currently includes 15 different planetary objects, with Callisto and Europa representing the latest additions (Vorburger & Wurz, 2018; Vorburger et al., 2015, 2019). In the study presented herein, a 3D version of the Monte-Carlo model was used to simulate the three plume models.

In this model, density profiles are calculated from the individual trajectories of a large number of sample particles simulated independently. Initial conditions are randomly sampled from the energy and angular distributions describing the chosen release process (see Vorburger et al., 2015 for mathematical descriptions of the release processes). In our Monte-Carlo model, particles are part of a thermal distribution, described by a Maxwell-Boltzmann velocity distribution, and assumed to be collision-free, that is, their trajectories are computed independently. In reality, the particles that constitute the plume experience some collisions close to the source (up to a few kilometers). Since we are not interested in the source-region, though, but rather in the extended exosphere (where the plumes were observed), we analytically account for the collisional part of the atmosphere (see. e.g., Bauer & Lammer, 2004), and apply our model to the collision-less regime of the plume. See also Section 7 for more justification of this assumption. For the future, it is planned to replace the analytical section with a Discrete Simulation Monte-Carlo (DSMC) model.

4.1. Plume Model

In our model we implement two plume sources, one located at 180°W/55°S the other located at 80°W/75°S. The key parameters of the plumes observed by Roth, Saur, et al. (2014) were presented in Section 2 and in Table 1. Most notably, the H_2O molecules need to rise 200 ± 100 km high, exhibit a latitudinal expansion of ~20°, and result in an observed tangential column density of ~$1.5 \cdot 10^{16}$ cm^{-2} in a 225 km × 225 km pixel. In each model, the source area of the plume thus needs to be dimensioned to satisfy these conditions (the scale height is given by the release process and thus results from the parameters of the chosen release process). As in Section 3, we present the implementation details for the three plume models in individual paragraphs, and give an overview of the models' key parameters in Table 2.

4.1.1. Model 1: Near-Surface Liquid Inclusions

Surface evaporation of a liquid can be modeled in a straight forward manner, with the vapor pressure governing the particles' release process. The release velocity can be sampled from a thermal velocity distribution, the temperature of which is equal to the water reservoir temperature. For the surface liquid H_2O temperature we chose the triple point temperature of 273.16 K. The corresponding mean thermal velocity is $(8k_BT/(\pi m))^{1/2}$, with k_B = Boltzmann constant, T = 273.16 K, and m = 18 amu, which is equal to 567 m/s. At 273.16 K the water vapor pressure is 612 Pa, resulting in a particle release flux of ~$9 \cdot 10^{21}$ cm^{-2}s^{-1}. With

this release flux, to obtain a total water content of (4.9–8.2) · 10^{31} molecules in a 225 km × 225 km pixel, the reservoir surface area needs to be equal to ~300 m^2 (which corresponds to a reservoir diameter of ~20 m assuming a circular reservoir shape).

4.1.2. Model 2: Diapirs

As mentioned in Section 3, for diapirs, temperatures on the order of 210–270 K are usually proposed (though temperatures might in theory be as low as 86 K), with 250 K being the most frequently suggested Europa diapir temperature. At these temperatures, the H_2O molecules are in a liquid or frozen state, depending on the water composition (i.e., depending on the content of dissolved species, e.g., $MgSO_4$ and/or Na_2SO_4, which act as anti-freeze agents). As in the liquid inclusion model, diapir particle release is governed by the temperature-dependent water vapor pressure. With the 270 K diapir plume being very similar to the 273.16 K liquid inclusion plume, we omit modeling such a diapir and instead implement diapirs with three lower temperatures: 150 K (the mean temperature between the minimum surface ice temperature and the minimum melting temperature for salty ice), 210 K (the minimum melting temperature for salty ice), and 250 K (the favored diapir temperature). Corresponding thermal release velocities range from 420 to 542 m/s. Again, we compute the required reservoir areas to obtain the same total water content Roth, Saur, et al. (2014) determined from their observation, and obtain diapir surface areas of 3.14e10 m^2 (diameter = 200 km), 2.83e5 m^2 (diameter = 600 m), and 2,830 m^2 (diameter = 60 m) for the three temperatures. Out of these three values, the dimension of the 210 K diapir agrees best with the typical diapir radii of 2–4 km mentioned in Section 3.

4.1.3. Model 3: Oceanic Plumes

As mentioned in Section 3, the icy crust situated on top of the liquid water ocean forces a hydrostatic pressure onto the water below, the magnitude of which depends on the ice shell thickness, the density of the ice, and Europa's gravitational acceleration. For an ice shell thickness of 25 km, a surface gravity of 1.314 m/s^2, and an ice density of 918 kg/m^3 we compute a hydrostatic pressure of ~300 bar at the bottom of the ice shell. At 300 bar, water exists in its liquid form at temperatures higher than ~270 K but at the top of the water in the crack it will be around the triple point temperature. We accordingly chose 270 K as the ocean temperature for this model. This also agrees well with the assumption that dissolved species are present in the water ocean that lower the freezing-temperature to a value slightly below the triple point. As the crack opens, a water column will rise until it reaches an equilibrium water level ~700 m below the ice surface. If the conduit remains open (does not freeze shut), this will be the height from which water vapor escapes into space.

As mentioned in Section 3, the particles in the oceanic plume model might behave more like a temperature-driven vapor (thermal plume) or more like a jet (jet plume), depending on the conduit's geometry. If the conduit results in a thermal plume, the plume can be modeled in a similar fashion as in the previous two cases, though with a narrowed angular expansion arising from the geometric restrictions imposed by the flow through the conduit. It is known from gas flows in the collisional regime through structures with a large aspect ratio that the angular distribution at the exit is narrower than for unobstructed flow (Rugamas et al., 2000). To accomplish this, we narrowed the angular emission from a hemisphere for the unobstructed thermal emission (a cosine angular dependence in elevation) to a more narrow distribution in elevation angle (with a cosine^20 angular dependence in elevation). This increased the average ejection angle from ~60° to ~80° (measured from the surface plane), the average angle under which particles are ejected from a conduit of the given dimensions. The narrowing of the angular distribution results in the tangential velocity being lowered to about one third of the nominal value (see the reduced v_{tan} in Table 2).

If the conduit exhibits a converging-diverging geometry, it might function as a de Laval nozzle (facilitating an isentropic expansion into vacuum), resulting in a supersonic jet. Then, the typical velocity of a jet plume particle can be computed from $v_{tot} = \sqrt{(2 \cdot n \cdot R \cdot T_s \cdot cp/cv)/(m \cdot [cp/cv - 1])}$, where n is the mass fraction of the gas in the eruptive material (set to 1 here to maximize the velocity [see also the note in the next paragraph]), R is the ideal gas law constant, T_s is the temperature of the gas (270 K), cp/cv is the isentropic expansion factor of water (equal to 1 + 2/f ~1.33, with f being the degrees of freedom [6 in case of H_2O]; cf., Thompson & Sonin, 1973), and m is the molecular mass of water (cf. Fagents et al., 2000). For the jet implementation of the oceanic plume model, this equation results in a typical ejection velocity of ~1,100 m/s. Again, due to the flow through the narrow conduit geometry, the tangential velocities of these particles are reduced, resulting in an average launch angle of ~80° with respect to the surface plane.

Table 3
Reaction Rates and Emission Fractions for H_2O Pathways That Eventually Lead to Either a Lyman-α or an OI 130.4 nm Emission

Pathway	Rate (s^{-1})→Product	Rate (s^{-1})→Product	Rate (s^{-1})→Product	Fraction
1	2.09e-08→Ly-α			2e-05
2	9.06e-10→OI			8e-07
3	5.25e-06→H	8.18e-05→Ly-α		7e-05
4	5.49e-07→O	5.72e-07→OI		1e-06
5	5.22e-06→OH	5.71e-06→H	8.18e-05→Ly-α	3e-06
6	5.22e-06→OH	5.71e-06→O	5.72e-07→OI	5e-07
7	2.22e-07→ H_2	3.88e-08→Ly-α		3e-09
8	2.22e-07→ H_2	1.83e-07→H	8.18e-05→Ly-α	5e-10

Note that the two cases we present herein are the two extreme cases for oceanic plumes, with the jet plume representing the most energetic oceanic plume type, and the thermal plume representing the least energetic oceanic plume type. A realistic plume will probably have a profile somewhere in between the two profiles modeled herein.

As in the previous two models, an appropriate reservoir (conduit) area needs to be determined. Assuming a release flux of $\sim 7 \cdot 10^{21}$ $cm^{-2}s^{-1}$ (the sublimation flux computed for a temperature of 270 K), we compute a required conduit area of ~380 m^2 (diameter = 22 m), which is in good agreement with the probable conduit widths of 1–100 m, as reviewed in in Section 3.

4.2. Lyman-α and OI 130.4 nm Emission Mechanisms

Once water exists in its gaseous form, it can be dissociated by UV photons and electrons into H and O atoms, either directly or via the fragment molecules OH and H_2. The water molecules themselves are hard to detect in their ground state, but the atomic fragments H and O can emit strong Lyman-α and OI 130.4 nm lines, and are thus often used as proxies for the underlying water abundance. Table 3 lists different pathways that can lead to either Lyman-α or OI 130 nm emission lines. Note that in some pathways excitation occurs during the dissociation (dissociative excitation) whereas in other pathways excitation occurs without dissociation (resonant photon scattering or electronic excitation). In the following, we present the different pathways in detail, and also describe how we determined the associated rates.

In pathways 1 and 2 (see Table 3) dissociative excitation of H_2O directly results in the emission of Lyman-α and OI 130.4 nm lines. This can only occur through the interaction of water molecules with electrons. Photons can dissociate water molecules as well, but do not result in dissociative excitation (cf. http://phidrates.space.swri.edu). The emission rates for pathways 1 and 2 thus only depend on the water molecule abundance, the electron flux, and the water-electron dissociative excitation cross section. The water molecule abundances are taken from our model results (see Section 5). The differential electron flux has been reviewed by Jun et al. (2019), and exhibits a maximum of ~1e7 $cm^{-2}s^{-1}sr^{-1}eV^{-1}$ at a few eV, while the energy-dependent dissociative excitation cross sections for water molecules interacting with electrons can be obtained from Makarov et al. (2004), and is on the order of ~1e-17 cm^2 for Lyman-α and ~1e-19 cm^2 for OI 130.4 nm around 100 eV. Integrating over energy results in Lyman-α and OI 130.4 nm emission rates of 2.09e-08 s^{-1} and 9.06e-10 s^{-1} for pathways 1 and 2, respectively.

Pathways 3 and 4 involve dissociation of H_2O that results in ground state H and O atoms, which can then emit Lyman-α or OI 130.4 nm through either electronic excitation or through resonant photon scattering. Ground state H and O are produced at rates of 5.25e-6 s^{-1} and 5.49e-7 s^{-1}, respectively, according to Huebner et al. (1992), http://phidrates.space.swri.edu, electron fluxes mentioned above, and cross section measurements presented by Darrach and McConkey (1993); Müller et al. (1993); Itikawa and Mason (2005); McConkey et al. (2008). To compute the electron excitation rates for H and O, the electron flux that was used for pathways 1 and 2 can be used here as well. The electron excitation cross sections of H and O are on the order of ~1e-16 cm^2 for Lyman-α and ~1e-17 cm^2 for OI 130.4 nm according to Rountree and Henry (1972); Gulcicek and Doering (1988); Laher and Gilmore (1990); Zatsarinny and Tayal (2002); Johnson et al. (2003, 2005). Integrating over energy results in Lyman-α and OI 130.4 nm emission rates of 4.11e-7 s^{-1} and 7.58e-8 s^{-1}, respectively. The UV resonant scattering rates can be directly taken from Huebner et al. (1992) and http://phidrates.space.swri.edu, and are equal to 8.14e-5 s^{-1} and 4.96e-7 s^{-1}, respectively.

Pathways 5 through 8 are similar to pathways 3 and 4, but include an additional step, either via OH or via H_2. The dissociation rates that produce OH and H_2, as well as the further dissociation rates into H and O can be computed from the electron and photon fluxes already mentioned, and from the interaction specific cross sections which are on the order of $\sigma_{H_2O\rightarrow OH}$ ~1e-16 cm^2 (Darrach & McConkey, 1993; Itikawa & Mason, 2005; McConkey et al., 2008; Müller et al., 1993), $\sigma_{H_2O\rightarrow H_2}$ ~1e-17 cm^2 (by analogy), $\sigma_{OH\rightarrow H,O}$ ~1e-16 cm^2 (Chakrabarti et al., 2019), $\sigma_{H_2\rightarrow H}$ ~1e-16 cm^2 (Chung et al., 1975), and $\sigma_{H_2\rightarrow Lyman-\alpha}$ ~1e-17 cm^2 (Chung et al., 1975). Integrating over energy, one obtains OH and H_2 creation rates of 5.22e-6 s^{-1} and 2.22e-7 s^{-7},

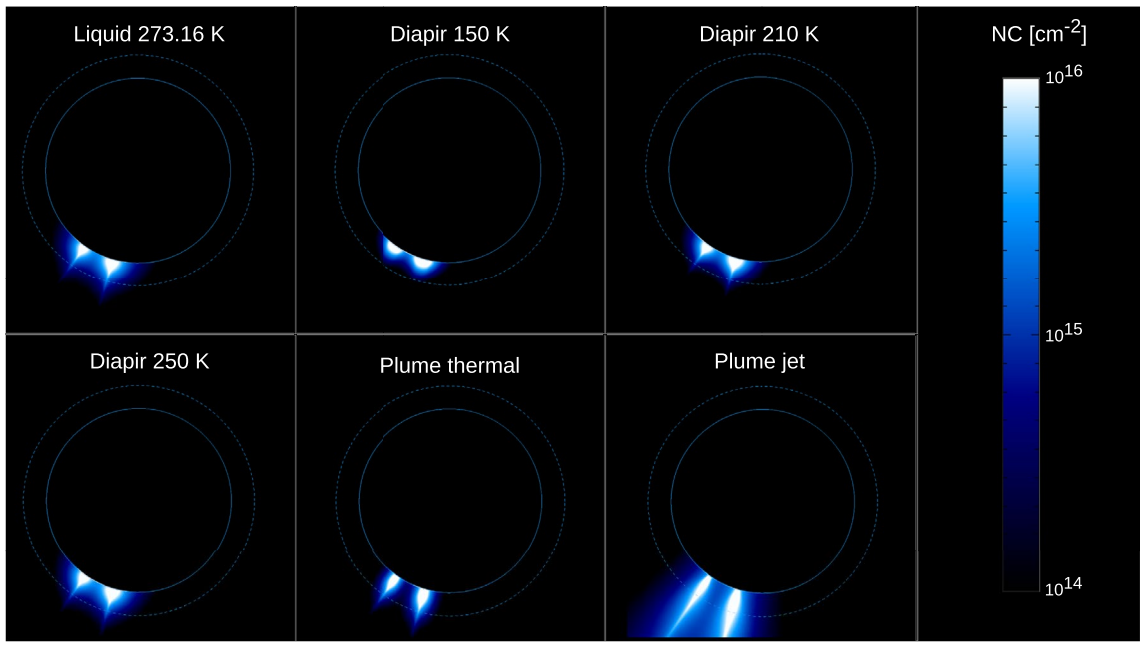

Figure 2. H_2O tangent column density profiles for the three models investigated shown on a logarithmic scale in high resolution (24 km × 24 km). Shown are the model results for a near-surface liquid inclusion, diapirs at three different temperatures, and an oceanic thermal as well as jet plume.

respectively, and further H and O creation rates of 5.71e-6 s^{-1} (H and O from OH) and 1.83e-7 s^{-1} (H from H_2), as well as 3.88e-8 s^{-1} direct Lyman-α emission from H_2. Once ground state H and O has been produced, Lyman-α and OI 130.4 nm can again be emitted through photon resonant scattering and electron excitation as already described for pathways 3 and 4.

Table 3 lists all pathways and the associated emission and dissociation rates. Comparison of the individual pathways' overall resulting emission rates is not straight forward, though. The problem here is that the rates given in the different columns act on different populations that have different residency times. Take pathway 3, for example, The first rate given (5.25e-6 s^{-1}) acts on the originally released H_2O molecules, whereas the second rate (8.18e-5 s^{-1}) acts on the produced H fragments, with both populations exhibiting different residency times. To be able to compare the efficiency of the different pathways we thus computed a new product, the fraction of original H_2O molecules that will eventually lead to either a Lyman-α or OI 130.4 nm emission (presented in the last column of Table 3). These fractions take into account on which population the given rates act, and how long the residency times of these populations are. The residency times themselves were obtained from our simulations, and range from a few hundred seconds (H_2O molecules, H_2, and H fragment)s to a few thousand seconds (OH and O fragments).

In our model, all of these pathways and the associated rates are implemented to their full extent for each model case. If a particle emits either Lyman-α or OI 130.4 nm, the emission is recorded and the simulation of that particle is stopped. If a particle is dissociated, the dissociation products are simulated henceforth, until they themselves either emit Lyman-α or OI 130.4 nm or until they meet another stopping criterion (e.g., escape or surface adsorption).

5. Simulation Results

5.1. H_2O

Figure 2 shows the column density profiles for the H_2O molecules released by the near-surface liquid inclusion model, three diapir models with different temperatures (150, 210, and 250 K), the oceanic thermal plume model, and the oceanic jet plume model, all displayed on a logarithmic scale. The excerpts shown reach from Europa's center to 670 km above Europa's surface, at a resolution of 24 km × 24 km per pixel.

Table 4
Plume H_2O Model Results: $NC^{(1)}$ = Tangent Column Density in a 24 km × 24 km Pixel Resolution, $NC^{(2)}$ = Tangent Column Density in a 225 km × 225 km Pixel Resolution, and H = Scale Height

	Observation	Liquid inclusion	Diapir 150 K	Diapir 210 K	Diapir 250 K	Plume thermal	Plume jet
$NC^{(1)}$ (10^{17} cm^{-2})	-	4.0	1.1	5.5	4.9	6.5	2.4
$NC^{(2)}$ (10^{16} cm^{-2})	1.5	1.5	1.6	1.6	1.8	1.8	1.5
H (km)	200 ± 100	118	68	90	103	180	510

The view is the same that was used for Figures 2 and 3 in Roth, Saur, et al. (2014), that is, the Sun is out of the paper plane (in the direction of the viewer), while Jupiter is located to the right. The blue solid circles denote Europa's surface, whereas the blue dashed circles indicate the HST bin radial extent (i.e., 390 km above Europa's surface), shown to facilitate visual comparison with the Roth, Saur, et al. (2014) measurements. Table 4 summarizes the model results and compares them to the Roth, Saur, et al. (2014) observation (given in the first column).

The temperature of the near-surface liquid inclusion plume was set to 273.16 K, that is, the triple point temperature of water. The corresponding mean thermal velocity equals 567 m/s, which leads to a scale height of 118 km, and we obtain a surface tangent column density of $4 \cdot 10^{17}$ cm^{-2} in a 24 km × 24 km resolution image. Note that this column density is by a factor of more than 10 higher than the column density computed by Roth, Saur, et al. (2014). The reason for this discrepancy is that Roth, Saur, et al. (2014) observed the plume in a much lower resolution than modeled herein (75 km × 75 km), and presented their images in an even lower resolution of 225 km × 225 km per pixel. Roth, Saur, et al. (2014) thus most probably present an average of the whole canopy produced by the plume (see Berg et al., 2016), whereas we sample the plume at much higher resolution. If we average our results over the same area as Roth, Saur, et al. (2014) uses for their bins (i.e., 225 km by 225 km) we obtain a column density of $1.5 \cdot 10^{16}$ cm^{-2}, that is, the same value Roth, Saur, et al. (2014) obtain.

For the diapirs we modeled 3 different temperatures: 150, 210, and 250 K. The scale heights of the modeled plumes are 68 km, 90 km, and 103 km, respectively, comparable to, though somewhat lower than, the scale height obtained by Roth, Saur, et al. (2014). The column densities in a 24 km × 24 km pixel are on the order of (1–6) × 10^{17} cm^{-2}, which translates to values of (1.6–1.8) · 10^{16} cm^{-2} in a 225 km × 225 km resolution.

Finally, the lower middle and right excerpts show the model results of the oceanic plume models (middle panel = thermal plume model, right panel = jet plume model). In both cases the ejection angle is equal to ~80°, but whereas the total velocity of the thermal plume is comparable to the non-oceanic total velocities, the total velocity of the jet plume is twice as high (and supersonic). The scale heights associated with the plumes are equal to 180 km in the thermal case, and 510 km in the jet case, and the column densities in a 24 km by 24 km pixel resolution are 6.5×10^{17} cm^{-2} and 2.4×10^{17} cm^{-2}, respectively. Again, down-sampling results in column densities of 1.8×10^{16} cm^{-2} and 1.5×10^{17} cm^{-2} in a 225 km × 225 km pixel resolution.

Overall, the morphologies of the plumes show two distinct plume sources in all scenarios. As for the individual plumes, the higher the temperature of the supply reservoir, the higher their scale height. Since the canopy of the particles falling back to the surface is much broader than the plume's center (i.e., the region of the upward traveling particles; see also Berg et al., 2016), there is no difference discernible in the width of the non-oceanic plumes, even though their supply reservoir areas vary by several orders of magnitude. The two oceanic plumes are similar in shape but narrower than the non-oceanic plumes (by design). In addition, the jet plume reaches much higher altitudes (on the order of 500 km) than either the thermal plume (on the order of 200 km) or the non-oceanic plumes (~70–120 km). The tangent column densities of the modeled plumes in low resolution all agree very well with the tangent column densities inferred by Roth, Saur, et al. (2014) from their measurements. This is not surprising, as we set the supply region area to meet this condition.

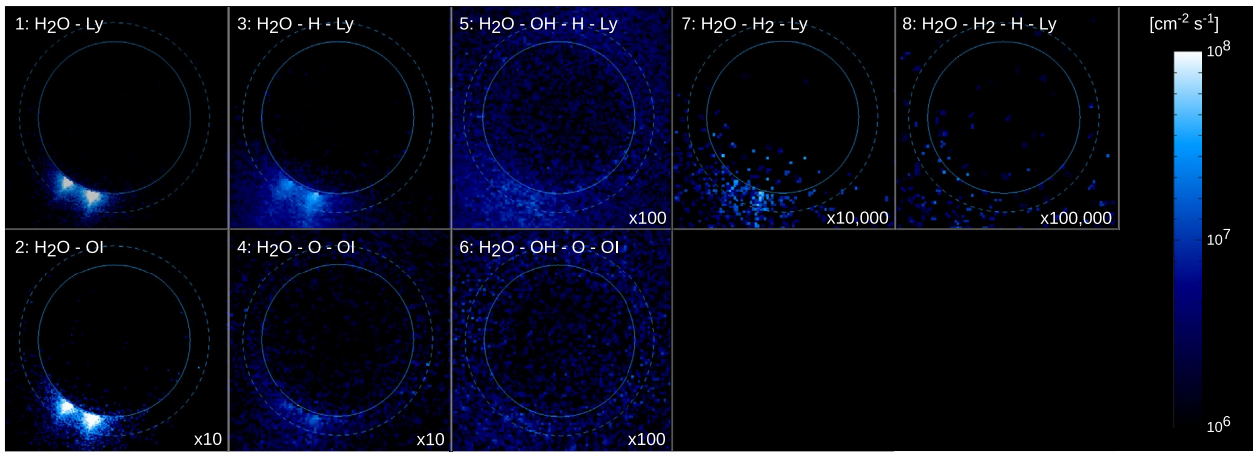

Figure 3. Liquid inclusion model Lyman-α and OI 130.4 nm emission profiles for the eight pathways presented in Table 3. Note that some emission profiles had to be enhanced (by a factor of 10–100,000) to be visible on the same scale.

5.2. Lyman-α and OI 130.4 nm Emission Profiles

As mentioned in Section 4.2, water molecules themselves are hard to detect, so the hydrogen and oxygen related Lyman-α and OI 130.4 nm emission lines are often used as proxies. Table 3 lists all pathways that eventually can result in either a Lyman-α or an OI 130.4 nm emission. In our model we implemented all these pathways using the corresponding rate constants, and determined for each model the resulting overall Lyman-α and OI 130.4 nm emission profiles.

Figure 3 shows the emission profiles of the individual pathways for the liquid inclusion model. The top row presents pathways 1, 3, 5, 7, and 8, all of which eventually can result in a Lyman-α emission. To be able to compare the different Lyman-α emission profiles some images had to be enhanced, see the lower right corner of each image for enhancement factors. The bottom row shows the OI 130.4 nm emission profiles of pathways 2, 4, and 6. Again, applied enhancement factors necessary to show these images on the same scale as the Lyman-α images are shown in the lower right corners. Overall, the applied enhancement factors reflect the fraction of initial H_2O particles that eventually will lead to an emission given in the last column of Table 3.

Note that the emission fluxes presented in Figure 3 were not computed analytically, but rather by simulating the full pathways (i.e., tracing particles, including dissociation products, until they either emit a line or meet another stopping criterion). This was necessary because some of the particles (especially of the higher-numbered pathways) do not start their trajectories at the plume source region, but rather at the predecessor particle's break-up position, which cannot be determined analytically since the break-up process is of stochastic nature. In addition, the dissociation products start their individual trajectories with vastly different initial velocities, that is, the sum of the velocity they inherit from the predecessor particle plus a fraction of the excess energy released during break-up.

It is clear from these images, that whereas direct H_2O dissociative excitation emissions (pathways 1 and 2) and emissions occurring after only one dissociation step (pathways 3, 4, and 7) still resemble the original plumes' structures, information on the plume locations has almost completely vanished in the pathways where more than one dissociation step is involved (5, 6, and 8). In addition, pathways 1 through 4 are mainly responsible for the total Lyman-α and OI 130.4 nm emission profiles. It is noteworthy, that whereas the rates of pathways 3 and 4 are higher than the rates of pathways 1 and 2, respectively, the emissions they produce are overall fainter, because they are distributed over much larger areas. Pathways 5 through 8 only contribute very little to the overall emission profiles, and accordingly had to be significantly enhanced to be visible at all on the same scale.

Figures 4 and 5 present the total Lyman-α and OI 130.4 nm emission profiles of all 6 models analyzed. To be able to compare our modeled high resolution emission profiles to the Roth, Saur, et al. (2014) observations, we had to apply an image post-processing algorithm that mimicks the HST/STIS observational constraints.

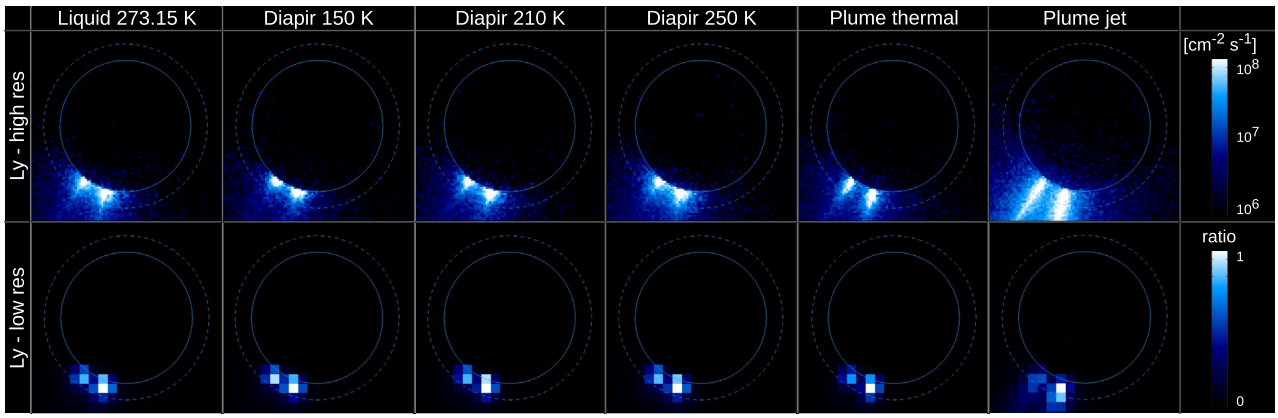

Figure 4. Simulated Lyman-α emission flux of all six models investigated. The top row shows the profiles on a logarithmic scale with a resolution of 24 km × 24 km and the bottom row shows the profiles on a linear scale with a resolution of 225 km × 225 km normalized to the brightest pixel after having introduced a jitter (see text). Note that the top colorbar of this figure is different from the top colorbar in Figure 5.

Roth, Saur, et al. (2014) state that their original pixel size is 75 km × 75 km, with systematic uncertainties of the disk location by 1–2 pixels. These disk location uncertainties introduce uncertainties in the derived height and radial profile of about 100 km. Additionally, in their Figure 3, to enhance visibility of the significant features, Roth, Saur, et al. (2014) re-binned their pixels into 3 × 3 pixel bins (resulting in bin sizes of 225 km × 225 km). To implement this data processing algorithm in our modeling, we re-bin our 24 km × 24 km pixels into pixels of size 75 km × 75 km, introduce a jitter with a standard deviation of $\sigma = 100$ km (mimicking the disk location uncertainty during the extended observation time), and re-bin the data to exhibit a spatial resolution of 225 km × 225 km. Whereas the top rows of Figures 4 and 5 show the emission profiles on a logarithmic scale with the original high spatial resolution of 24 km × 24 km, the bottom rows show the profiles after application of the post-processing algorithm, that is, with the lowered resolution of 225 km × 225 km, on a linear scale, and normalized to the brightest pixel (to allow comparison to the Roth, Saur, et al., 2014 images).

Similarly to Figure 2, structural differences in the 6 different models are noticeable in the high-resolution emission profiles displayed on a logarithmic scale: lower energetic models result in radially more confined plumes, and the oceanic plumes are narrower than the non-oceanic plumes. While all lower-resolution images still capture the dual nature of the plume sources, other differences (e.g., scale height and lateral expansion) have mostly vanished. This is due to the lower resolution being unable to resolve the fine-scaled structure of the plume, especially with an introduced jitter. The emission profiles of all models, except the

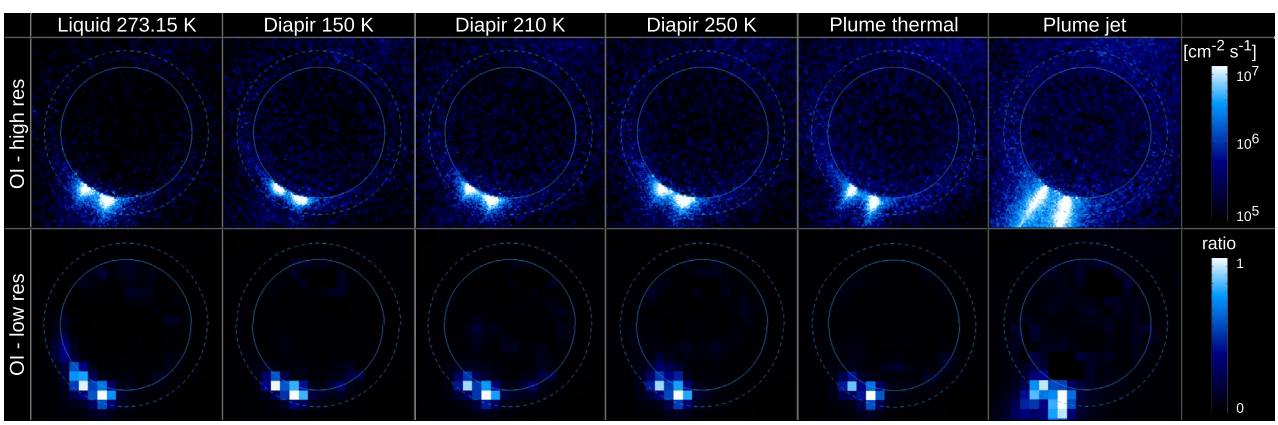

Figure 5. Simulated OI emission flux of all six models investigated. The top row shows the profiles on a logarithmic scale with a resolution of 24 km × 24 km and the bottom row shows the profiles on a linear scale with a resolution of 225 km × 225 km normalized to the brightest pixel after having introduced a jitter (see text). Note that the top colorbar of this figure is different from the top colorbar in Figure 4.

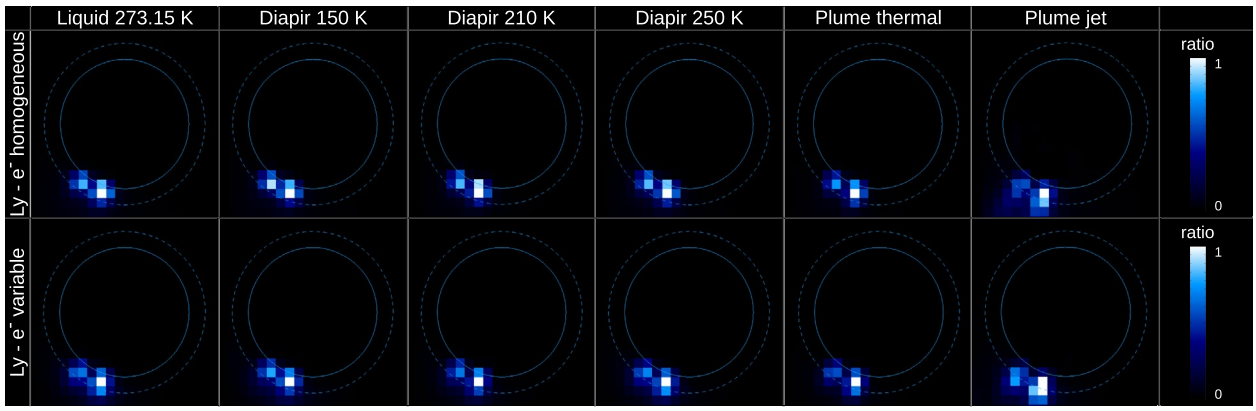

Figure 6. Simulated low-resolution Lyman-α emission profiles assuming a homogeneous electron environment (top row) and a variable electron environment (bottom row). For the variable electron environment, electron properties along the sub-plasma line as presented in Rubin et al. (2015) are used.

oceanic jet model, are thus visually virtually indistinguishable. The oceanic jet profile with its large scale height is the only model that is clearly distinguishable from the other models, even in low resolution. As mentioned in Section 4.1, though, this jet plume is an extreme case. A more realistic oceanic plume will probably exhibit a profile somewhere between the thermal plume and the jet plume.

Assuming a homogeneous electron environment in the vicinity of the plumes presents an over-simplification. In reality, the plasma parameters close to Europa will be quite variable, especially in the near surface environment. To present a more realistic scenario, we thus decided to implement variable electron densities, velocities, and temperatures, as presented in Rubin et al. (2015). In general, as the plasma approaches the surface, electron densities and velocities increase, while electron temperatures decrease. Unfortunately, Roth, Saur, et al. (2014) write that the longitudinal plume source locations cannot be determined from the images. For our simulations, we thus chose to implement electron properties along the sub-plasma line, which experience the highest variations in the x-y plane according to Rubin et al. (2015). In this configuration, the densities, velocities, and temperatures each vary by more than a factor of 10 within the first ~500 km, resulting in the emission rates also varying by a factor of >10 in said altitude range. Figure 6 compares the low-resolution Lyman-α emission profiles for the homogeneous electron environment (top row) with the low-resolution Lyman-α emission profiles for a variable electron environment (bottom row). The combination of increasing electron densities and velocities but decreasing electron temperatures with decreasing altitude results in the maximum Lyman-α emission location being shifted to slightly higher altitudes. Since all models experience the same variation in electron properties, though, the six models remain equally similar among themselves. As mentioned above, Roth, Saur, et al. (2014) state that the longitudinal plume source location is unknown. We thus decided to use the homogeneous electron environment throughout this study, as choosing a variable electron environment without knowing the correct configuration would introduce an additional potential source of error in our analyses.

Figure 7 compares the simulated Lyman-α and OI 130.4 nm emission profiles of the liquid inclusion model to the measured Lyman-α and OI 130.4 nm emission brightness profiles presented by Roth, Saur, et al. (2014). We chose to present this model for visual comparison because it is energetically a good sample case, that is, neither extremely energetic nor extremely low in energy. As mentioned previously, like the measurements, the models are normalized to the brightest pixel to facilitate visual comparison. Note, though, that on an absolute scale, the Lyman-α model emission are about 10 times brighter than the OI 130.4 nm model emissions (see Figure 3). This is also the case in the Roth, Saur, et al. (2014) observations, where the colorscale for the Lyman-α emission brightness is 10 times higher than the colorscale of the OI 130.4 nm emission brightness. Also, while our models only include plumes as emission sources, the observations naturally contain all emission sources present, that is, also emissions from the global atmosphere, any other transient atmosphere that might have been present at the time, and any background. By visual comparison, the model images agree quite well with the observations. The radial and lateral extents seem to agree with the observations, as does the fact that two plume sources are distinguishable in both images.

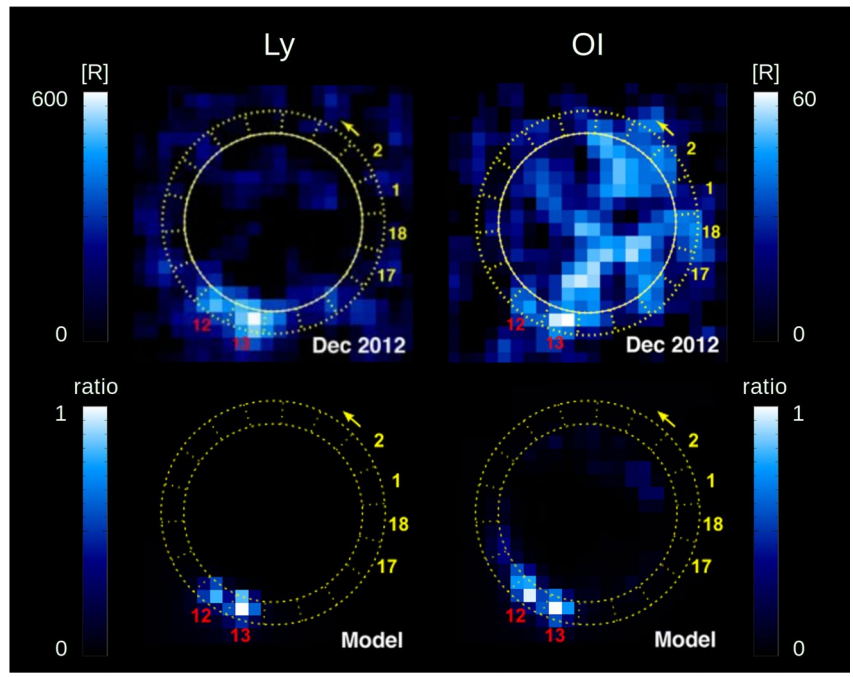

Figure 7. Comparison between the Lyman-α and OI 130.4 nm emission profiles measured by Roth, Saur, et al. (2014) (top row) and modeled for the liquid inclusion plume model (bottom row). Note that since we compare images with different physical units (Rayleighs vs. $cm^{-2}s^{-1}$) and accordingly with different ranges, the colorbar of the modeled profiles were normalized to the brightest pixel. In addition, to facilitate comparison between the observation and the model, the bins used by Roth, Saur, et al. (2014) are depicted by dashed yellow lines (inner circle = Europa's surface, outer circle = 390 km above Europa's surface, bin width = 545 km at the surface).

Finally, in Figure 8 we compare the (normalized) modeled Lyman-α and OI 130.4 nm annular limb (left) and radial (right) emission profiles with the Lyman-α ad OI 130.4 nm emission profiles presented by Roth, Saur, et al. (2014). In our model profiles, shown by the asterisks, we present the averages over the six individual model results, whereas the vertical ranges denote the minimum and maximum values obtained. Since the models were normalized to the brightest pixel, there is no range associated with bin 13, the bin where the normalization was made. The annular limb profiles of both the observations and the models clearly show that the plumes are mostly confined to bins 12 and 13, with some surplus emissions in the neighboring bins. The radial observation and model profiles (which only contain data from bins 12 and 13) show that the plume emission maxima are not located at the surface itself, but rather at 100–200 km altitude. This is a result of the stochastic nature of the emission process, that is, the emission occurring at any random position along the particle trajectory.

6. Discussion

The six scenarios of the three different plume types implemented all agree well with the plume observations presented by Roth, Saur, et al. (2014). In all images shown in Figure 2, two distinct plume sources are visible in the H_2O profiles. Their tangential column densities in a 225 km × 225 km pixel resolution lie between $1.5 \cdot 10^{16}$ cm^{-2} and $1.8 \cdot 10^{16}$ cm^{-2}, values very close to the H_2O column density of $1.5 \cdot 10^{16}$ cm^{-2} computed by Roth, Saur, et al. (2014) based on their observations and interpretations. The scale heights of the non-oceanic plumes are on the order of 70–120 km, comparable to (though somewhat lower than) the radial extent of 200 km ± 100 km reported by Roth, Saur, et al. (2014). For the oceanic plumes, we implemented two extreme scenarios: The thermal plume resembles the lowest energetic plume type whereas the jet plume resembles the highest energetic plume type. The scale height of the thermal plume (180 km) agrees very well with the HST/STIS observations, while the scale height of the jet plume (510 km) is approximately twice the maximum value. As mentioned previously, a realistic plume probably exhibits

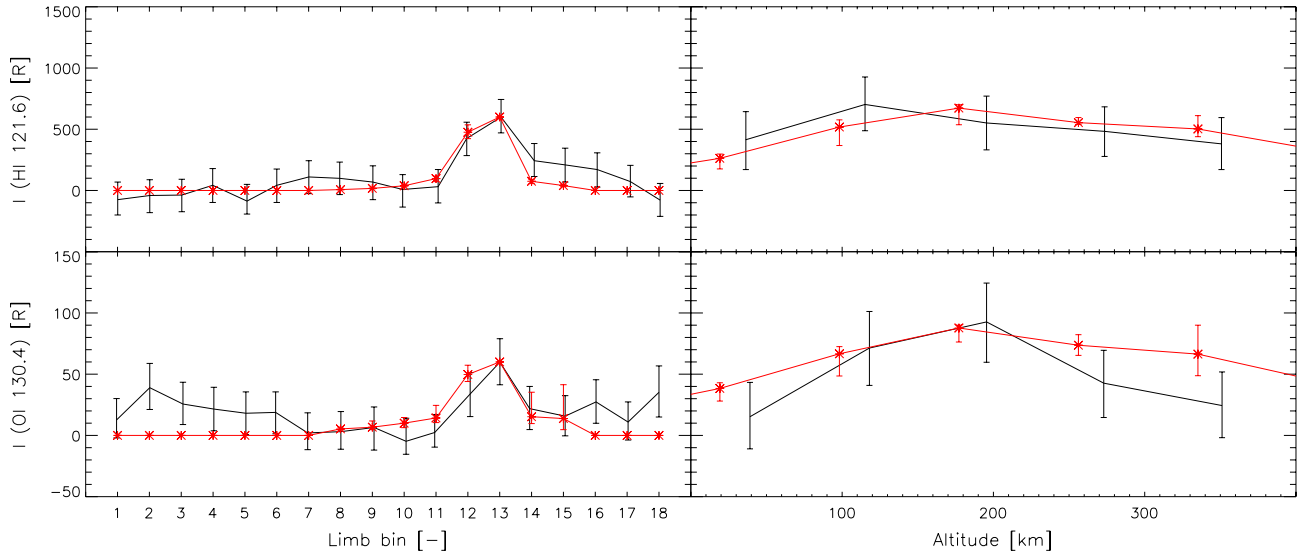

Figure 8. Lyman-α and OI 130.4 nm annular limb and altitude profiles from Roth, Saur, et al. (2014) (black) versus normalized modeled Lyman-α and OI 130.4 nm emission profiles (red; asterisks = average of all six models, vertical bar = [minimum, maximum] of all six models). The altitude profiles on the right contain only measurements from bins 12 and 13 (i.e., from the bins where plumes were identified). Since the data presented by Roth, Saur, et al. (2014) and our model results are not of the same unit, we normalized our data to the Roth, Saur, et al. (2014) data. This was done using bin 13, which does thus not exhibit a range. Note also the different *y*-axes used to present the measured Lyman-α and the OI 130.4 nm emission brightnesses.

a profile somewhere in between these two extrema. A more realistic oceanic plume would thus exhibit characteristics that agree very well with the characteristics Roth, Saur, et al. (2014) inferred from their observations.

We would like to emphasize again that whereas Roth, Saur, et al. (2014) measured Lyman-α and OI 130.4 nm emission profiles and used them as a basis to infer H_2O plume characteristics, we went about the problem the other way around. We first researched different possible plume sources, determined their physical characteristics, implemented these into our 3D Monte-Carlo model (without calibrating them to the observations, except for the source area), and finally compared the resulting plumes including their emission profiles to the plumes observed. Rather than sampling the complete possible parameter space, we thus set about first understanding the physics behind different plume sources, and then checking if they could provide a match to the available observations. Our results show that all plume sources are able to produce emission profiles similar to the observations, and that none of them can be disregarded solely based on the available plume observations.

In addition, we did not calculate the emission profiles analytically, but modeled them ab initio (see Table 3). This is necessary because already after one dissociation step determination of the initial position and velocity of a particle that will eventually result in a Lyman-α or a OI 130.4 nm emission is non-trivial. Our Lyman-α and OI 130.4 nm emission profiles were thus computed by implementing the full pathways (including none, one, or two stochastic dissociation processes) and are not based on the H_2O density profiles with added theoretical calculations.

Comparisons between the Lyman-α and OI 130.4 nm emission images presented by Roth, Saur, et al. (2014) and the emission profiles modeled herein also result in very good agreement. The structure and spatial extent of the modeled Lyman-α and OI 130.4 nm emission profiles are very similar to the structure and spatial extents of the observed emissions, especially when considering the overall patchiness of the observations (cf. Figure 7). The annular limb and altitude profiles of the six scenarios also perform well, containing clear plume signatures in bins 12 and 13 with some surplus emissions in the adjacent bins, and exhibiting emission maxima at an altitude of approximately 200 km (see Figure 7). The fact that the emission maxima are not located at, but at approximately one plume scale height above, the surface highlights the stochastic nature of the emission mechanism.

Analysis of the individual emission pathways (see Figure 3) shows that only pathways that include up to one dissociation step still reveal the original plume structures. Pathways including more than one dissociation step lead to more global particle distributions due to the large amount of released excess energy the dissociation products gain during each break-up process (a few eV vs. the initial kinetic H_2O energy of <0.1 eV). In addition, only pathways 1 through 4 contribute noticeably to the overall emission profiles (see the enhancement factors that had to be used in Figure 3 for pathways 5 through 8), and the Lyman-α emissions are about 10 times stronger than the OI 130.4 nm emissions. Finally, pathways 1 and 2 are the main producers of the emissions observed by Roth, Saur, et al. (2014). Even though pathways 3 and 4 lead to a higher fraction of H_2O molecules that eventually result in a Lyman-α or OI 130.4 nm emission (see last column in Table 3), the resulting profiles are fainter due to the profiles' more extended nature.

Figures 4 and 5 show in the bottom rows the linear low-resolution emission profiles of the six models analyzed. Whereas differences in the six emission profiles are clearly visible in the logarithmic high-resolution images (top rows), visual inspection shows that these differences have almost completely vanished once the image post-processing algorithm mimicking the HST/STIS observation capabilities has been applied. This is true for both a homogeneous and a variable electron environment. For a quantitative assessment of the similarity between the modeled and the observed images we performed an image correlation analysis that results in correlation coefficients >0.95 and >0.72 for the Lyman-α and OI 130.4 nm profiles of the first five models (correlation coefficient values range from −1 to 1, where ±1 indicates the strongest possible agreement and 0 the strongest possible disagreement). The oceanic jet plume correlation coefficient is on the order of 0.68 and 0.66 for the Lyman-α and OI 130.4 nm profile, respectively, values high, though not quite as high, as the correlation coefficients of the other models.

The correlation coefficients of the underlying high-resolution H_2O column density profiles (see Figure 2), on the other hand, range from 0.25 to 0.61, that is, clearly different enough to allow distinction. We thus conclude that one cannot determine from the Roth, Saur, et al. (2014) images what the physical nature of the observed plume was, which is only possible if the plume is observed in higher resolution or with a sufficiently large dynamic range (see Figure 3).

7. Conclusion and Outlook

Our analysis shows that the Lyman-α and OI 130.4 nm measurements as well as the inferred H_2O plume characteristics presented by Roth, Saur, et al. (2014) agree well with our current understanding of how plumes on icy worlds work. In this paper we analyzed three plume types (near-surface liquid inclusion, diapir, and oceanic) ab initio, with the area of the supply region being the only parameter set. All other parameters were determined according to the current best understanding of the underlying physical processes. The scale heights of all three investigated plume types agree well with the scale heights inferred from the HST/STIS observations (200 ± 100 km), as do the column densities. Concerning the plumes' morphologies, two plumes located about 500 km apart are distinctly visible in the H_2O column density as well as the Lyman-α and OI 130.4 nm emission profiles, even in images with resolutions as low as 225 km × 225 km per pixel, that is, the resolution Roth, Saur, et al. (2014) presented their measurements in.

The Roth, Saur, et al. (2014) observations have a resolution much lower than the expected collisional regime. In fact, the resolution and sensitivity of the observations are not sufficient to capture the collisional and the non-collisional part separately, and the non-collisional part (from a few km to ∼200 km) makes up on the order of 10–100 times more of the plume than the collisional part (reservoir surface up to a few km) does. We thus focused in this study on the collision-less regime (exospheric part of the plume), which is also the region that has been observed optically, and have accounted for near-surface collisions analytically. In the future, we plan on coupling our Monte-Carlo model with a DSMC model to capture the physics in the collisional part more thoroughly. This will allow us to not only investigate the near-surface regime more closely, but also to determine its effect on the extended non-collisional plume, and to include any other interactions (e.g., with particles originating from complex chemical interactions or other atmospheric sources) that might occur.

Modeling all possible Lyman-α and OI 130.4 nm emission pathways (see Table 3) results in Lyman-α and OI 130.4 nm emission profiles that have similar spatial expansions and reach similar altitudes as the H_2O

column density profiles. However, a key difference between the emission profiles and the column density profiles is that whereas the H_2O column density profiles' maxima are located at the surface, the emission profiles' maxima are located about one pixel (225 km) above Europa's surface. The fact that the emission maxima are not located at the surface but rather at one plume height above the surface was also observed by Roth, Saur, et al. (2014), and can be well explained by the stochastic nature of the emission process. Especially when one considers the fact that first order dissociation products, which start their trajectories at an arbitrary height within the plume and at high velocities, also play a non-negligible role in the overall emission profiles.

Overall, the modeled Lyman-α and OI 130.4 nm emission profiles of the three models investigated compare very well to the Lyman-α and OI 130.4 nm emission profiles measured by Roth, Saur, et al. (2014), both for a homogeneous and a variable electron environment. Based on our pathway analyses OI 130.4 nm emissions are about 10 times fainter than the Lyman-α emissions. This also agrees well with the Roth, Saur, et al. (2014) observations, who obtained emissions on the order of 600 Rayleigh for the Lyman-α emissions and 60 Rayleigh for the OI 130.4 nm emissions. What is noteworthy, though, is the fact that after having applied an image post-processing algorithm that mimicks the HST/STIS observation capabilities for the Europa observations, all three models produce almost identical emission profile images. Since none of the models contradict the Roth, Saur, et al. (2014) observations, and in fact all seem to match the observations equally well, it is impossible to infer from the currently available (low-resolution) observational HST/STIS data if the source of the plume observed by Roth, Saur, et al. (2014) is of oceanic nature or if it might be surficial.

Determination of the plume source is important, though, especially with respect to the ocean's potential to harbor life. Higher resolution images would provide a step in that direction. Optimally, though, a high-resolution mass spectrometer located on a spacecraft getting close to Europa would sample the plume material in situ for analysis. Europa Clipper (Phillips & Pappalardo, 2014), with its planned 44 flybys at altitudes ranging from 25 to 2,700 km, has a high chance of accomplishing this. In fact, the primary objectives of MAss Spectrometer for Planetary EXploration (MASPEX), the high-resolution mass spectrometer that will fly onboard the Europa Clipper mission to explore the habitability of Europa, are to determine the distribution of major volatiles and key organic compounds in Europa's exosphere/plumes including their association with geological features, and to determine the relative abundances of key compounds to constrain the chemical conditions of Europa's ocean (Waite et al., 2019). Besides Europa Clipper, also the JUpiter Icy moons Explorer (JUICE; Grasset et al., 2013) will encounter Europa, though at larger flyby distances of ~400 km. Even though the flyby distances are larger, if JUICE passes over a plume, the spacecraft is expected to receive enough signal to positively identify a plume in its data, given the plumes' scale heights presented in Table 4 (which was investigated in detail also by Huybrighs et al., 2017). The Neutral gas and Ion Mass spectrometer (NIM), one of six instruments of the Particle Environment Package (PEP) on board JUICE, could thus potentially also provide information on the chemical composition and the structure of Europa's plumes. Comparison between measurements and models of the plumes' density profiles and chemical compositions will allow us to determine the source of the observed plume. It is thus important to understand the different characteristics different plume types exhibit, to be prepared to interpret higher-resolution as well as in situ measurements correctly once they become available.

If the plumes truly are of oceanic nature, they provide a natural access to Europa's potential biosphere, and might even contain evidence of present or past life in form of bio-markers, for example, organic compounds, potential metabolic byproducts, isotopic abundance ratios of selected species (e.g., C and N), and certain functional groups (e.g., amides). These bio-markers could be detected by orbiting mass spectrometers, or by a medium (e.g., aerogel) that collects the plume material for subsequent analysis. Either way, plumes, be they of oceanic or of surficial origin, are definitely worth closer scrutiny.

Data Availability Statement

Data used to create Figures 2–8 presented in this study can be retrieved from Vorburger (2021).

Acknowledgment
A. Vorburger and P. Wurz gratefully acknowledge the financial support by the Swiss National Science Foundation.

References

Anderson, J. (2003). *Modern compressible flow: With historical perspective*. McGraw-Hill Education.

Arnold, H., Liuzzo, L., & Simon, S. (2019). Magnetic signatures of a Plume at Europa during the Galileo E26 Flyby. *Geophysical Research Letters*, *46*(3), 1149–1157. https://doi.org/10.1029/2018GL081544

Bauer, S. J., & Lammer, H. (2004). *Planetary aeronomy: Atmosphere environments in planetary systems*. Springer. https://doi.org/10.1007/978-3-662-09362-7

Berg, J. J., Goldstein, D. B., Varghese, P. L., & Trafton, L. M. (2016). DSMC simulation of Europa water vapor plumes. *Icarus*, *277*, 370–380. https://doi.org/10.1016/j.icarus.2016.05.030

Blöcker, A., Saur, J., & Roth, L. (2016). Europa's plasma interaction with an inhomogeneous atmosphere: Development of Alfvén winglets within the Alfvén wings. *Journal of Geophysical Research: Space Physics*, *121*(10), 9794–9828. https://doi.org/10.1002/2016JA022479

Brown, M. E., & Hand, K. P. (2013). Salts and radiation products on the surface of Europa. *The Astrophysical Journal*, *145*(4), 110. https://doi.org/10.1088/0004-6256/145/4/110

Carlson, R., Smythe, W., Baines, K., Barbinis, E., Becker, K., Burns, R., et al. (1996). Near-infrared spectroscopy and spectral mapping of Jupiter and the Galilean Satellites: Results from Galileo's Initial Orbit. *Science*, *274*(5286), 385–388. https://doi.org/10.1126/science.274.5286.385

Carlson, R. W., Anderson, M. S., Mehlman, R., & Johnson, R. E. (2005). Distribution of hydrate on Europa: Further evidence for sulfuric acid hydrate. *Icarus*, *177*(2), 461–471. https://doi.org/10.1016/j.icarus.2005.03.026

Carlson, R. W., Johnson, R. E., & Anderson, M. S. (1999). Sulfuric acid on Europa and the Radiolytic Sulfur Cycle. *Science*, *286*(5437), 97–99. https://doi.org/10.1126/science.286.5437.97

Carr, M. H., Belton, M. J. S., Chapman, C. R., Davies, M. E., Geissler, P., Greenberg, R., et al. (1998). Evidence for a subsurface ocean on Europa. *Nature*, *391*(6665), 363–365. https://doi.org/10.1038/34857

Cassen, P., Reynolds, R. T., & Peale, S. J. (1979). Is there liquid water on Europa? *Geophysical Research Letters*, *6*(9), 731–734. https://doi.org/10.1029/gl006i009p00731

Chakrabarti, K., Laporta, V., & Tennyson, J. (2019). Calculated cross sections for low energy electron collision with OH. *Plasma Sources Science and Technology*, *28*(8), 085013. https://doi.org/10.1088/1361-6595/ab364c

Chung, S., Lin, C. C., & Lee, E. T. P. (1975). Dissociation of the hydrogen molecule by electron impact. *Physical Review A (General Physics)*, *12*(4), 1340–1349. https://doi.org/10.1103/PhysRevA.12.1340

Clarke, C., & Carswell, B. (2007). *Principles of astrophysical fluid dynamics*. Cambridge University Press. https://doi.org/10.1017/CBO9780511813450

Cook, A. F., Shoemaker, E. M., Soderblom, L. A., Mullins, K. F., & Fiedler, R. (1982a). Volcanism in ice on Europa. *Bulletin of the American Astronomical Society*, *14*, 736–737.

Cook, A. F., Shoemaker, E. M., Soderblom, L. A., Mullins, K. F., & Fiedler, R. (1982b). *Volcanism in ice on Europa* (NASA Technical Memo, NASA TM-85127).

Dalton, J. B. (2007). Linear mixture modeling of Europa's non-ice material based on cryogenic laboratory spectroscopy. *Geophysical Research Letters*, *34*. https://doi.org/10.1029/2007GL031497

Dalton, J. B., Prieto-Ballesteros, O., Kargel, J. S., Jamieson, C. S., Jolivet, J., & Quinn, R. (2005). Spectral comparison of heavily hydrated salts with disrupted terrains on Europa. *Icarus*, *177*(2), 472–490. https://doi.org/10.1016/j.icarus.2005.02.023

Darrach, M., & McConkey, J. W. (1993). Absolute cross sections for dissociation of H_2O by electron impact. In T. Andersen, B. Fastrup, F. Folkmann, H. Kundsen, & N. Andersen (Eds.), *The physics of electronic and atomic collisions* (Vol. 295, pp. 811–819). https://doi.org/10.1063/1.45249

Fagents, S. A. (2003). Considerations for effusive cryovolcanism on Europa: The post-Galileo perspective. *Journal of Geophysical Research*, *108*(E12). https://doi.org/10.1029/2003JE002128

Fagents, S. A., Greeley, R., Sullivan, R. J., Pappalardo, R. T., Prockter, L. M., & Team, T. G. S. (2000). Cryomagmatic mechanisms for the formation of Rhadamanthys Linea, Triple Band Margins, and other Low-Albedo features on Europa. *Icarus*, *144*(1), 54–88. https://doi.org/10.1006/icar.1999.6254

Gaidos, E. J., & Nimmo, F. (2000). Planetary science: Tectonics and water on Europa. *Nature*, *405*(6787), 637–637. https://doi.org/10.1038/35015170

Giono, G., Roth, L., Ivchenko, N., Saur, J., Retherford, K., Schlegel, S., et al. (2020). An analysis of the statistics and systematics of limb anomaly detections in HST/STIS transit images of Europa. *The Astronomical Journal*, *159*(4), 155. https://doi.org/10.3847/1538-3881/ab7454

Granahan, J. C., Fanale, F. P., McCord, T. B., Hansen, G., Carlson, R., Kamp, L., et al. (1997). A Galileo Multi-Instrument Study of Europa's color heterogenieties. In *Aas/division for planetary sciences*. meeting abstracts #29.

Grasset, O., Dougherty, M. K., Coustenis, A., Bunce, E. J., Erd, C., Titov, D., et al. (2013). JUpiter ICy moons Explorer (JUICE): An ESA mission to orbit Ganymede and to characterise the Jupiter system. *Planetary and Space Science*, *78*, 1–21. https://doi.org/10.1016/j.pss.2012.12.002

Gulcicek, E. E., & Doering, J. P. (1988). Absolute differential and integral electron excitation cross sections for atomic oxygen. 5. Revised values for the $^3P \rightarrow {}^3S^0$ (1304 Å) and $^3P \rightarrow {}^3D^0$ (989 Å) transitions below 30 eV. *Journal of Geophysical Research*, *93*(A6), 5879–5884. https://doi.org/10.1029/JA093iA06p05879

Hanley, J., Dalton, J. B., III, Chevrier, V. F., Jamieson, C. S., & Barrows, R. S. (2014). Reflectance spectra of hydrated chlorine salts: The effect of temperature with implications for Europa. *Journal of Geophysical Research: Planets*, *119*(11), 2370–2377. https://doi.org/10.1002/2013JE004565

Helfenstein, S.-P., & Cook, A. F. (1984). Active venting of Europa?: Analysis of a transient bright surface feature. In *Lunar and planetary science conference* (pp. 354–355).

Huebner, W. F., Keady, J. J., & Lyon, S. P. (1992). Solar photo rates for planetary atmospheres and atmospheric pollutants. *Astrophysics and Space Science*, *195*(1), 1–294. https://doi.org/10.1007/BF00644558

Huybrighs, H. L. F., Futaana, Y., Barabash, S., Wieser, M., Wurz, P., Krupp, N., et al. (2017). On the in-situ detectability of Europa's water vapour plumes from a flyby mission. *Icarus*, *289*, 270–280. https://doi.org/10.1016/j.icarus.2016.10.026

Huybrighs, H. L. F., Roussos, E., Blöcker, A., Krupp, N., Futaana, Y., Barabash, S., et al. (2020). An active plume eruption on Europa during Galileo Flyby E26 as indicated by energetic proton depletions. *Geophysical Research Letters*, *47*(10). https://doi.org/10.1029/2020GL087806

Itikawa, Y., & Mason, N. (2005). Cross sections for electron collisions with water molecules. *Journal of Physical and Chemical Reference Data*, *34*(1), 1–22. https://doi.org/10.1063/1.1799251

Jia, X., Kivelson, M. G., Khurana, K. K., & Kurth, W. S. (2018). Evidence of a plume on Europa from Galileo magnetic and plasma wave signatures. *Nature Astronomy*, *2*, 459–464. https://doi.org/10.1038/s41550-018-0450-z

Jia, X., Kivelson, M. G., & Paranicas, C. (2021). Comment on "an active plume eruption on europa during galileo flyby e26 as indicated by energetic proton depletions" by huybrighs et al. *Geophysical Research Letters*, *48*(6). https://doi.org/10.1029/2020GL091550

Johnson, P. V., Kanik, I., Shemansky, D. E., & Liu, X. (2003). Electron-impact cross sections of atomic oxygen. *Journal of Physics B: Atomic and Molecular Physics*, *36*(15), 3203–3218. https://doi.org/10.1088/0953-4075/36/15/303

Johnson, P. V., McConkey, J. W., Tayal, S. S., & Kanik, I. (2005). Collisions of electrons with atomic oxygen: Current status (Vol 83, pg 589, 2005). *Canadian Journal of Physics*, *83*, 1071–1072. https://doi.org/10.1139/p05-061

Jun, I., Garrett, H. B., Cassidy, T. A., Kim, W., & Dougherty, L. (2019). Updating the Jovian electron plasma environment. *IEEE Transactions on Plasma Science*, *47*(8), 3915–3922. https://doi.org/10.1109/TPS.2019.2901681

Khurana, K. K., Kivelson, M. G., Stevenson, D. J., Schubert, G., Russell, C. T., Walker, R. J., & Polanskey, C. (1998). Induced magnetic fields as evidence for subsurface oceans in Europa and Callisto. *Nature*, *395*(6704), 777–780. https://doi.org/10.1038/27394

Kivelson, M. G., Khurana, K. K., Russell, C. T., Volwerk, M., Walker, R. J., & Zimmer, C. (2000). Galileo magnetometer measurements: A stronger case for a subsurface ocean at Europa. *Science*, *289*(5483), 1340–1343. https://doi.org/10.1126/science.289.5483.1340

Laher, R. R., & Gilmore, F. R. (1990). Updated excitation and ionization cross sections for electron impact on atomic oxygen. *Journal of Physical and Chemical Reference Data*, *19*(1), 277–305. https://doi.org/10.1063/1.555872

Loeffler, M. J., & Baragiola, R. A. (2005). The state of hydrogen peroxide on Europa. *Geophysical Research Letters*, *32*(17). https://doi.org/10.1029/2005GL023569

Makarov, O. P., Ajello, J. M., Vattipalle, P., Kanik, I., Festou, M. C., & Bhardwaj, A. (2004). Kinetic energy distributions and line profile measurements of dissociation products of water upon electron impact. *Journal of Geophysical Research*, *109*(A9). https://doi.org/10.1029/2002JA009353

McConkey, J. W., Malone, C. P., Johnson, P. V., Winstead, C., McKoy, V., & Kanik, I. (2008). Electron impact dissociation of oxygen-containing molecules A critical review. *Physics Reports*, *466*(1–3), 1–103. https://doi.org/10.1016/j.physrep.2008.05.001

McCord, T. B., Hansen, G. B., Fanale, F. P., Carlson, R. W., Matson, D. L., Johnson, T. V., et al. (1998). Salts on Europa's surface detected by galileo's near infrared mapping spectrometer. *Science*, *280*(5367), 1242–1245. https://doi.org/10.1126/science.280.5367.1242

McCord, T. B., Hansen, G. B., Matson, D. L., Jonhson, T. V., Crowley, J. K., Fanale, F. P., et al. (1999). Hydrated salt minerals on Europa's surface from the Galileo near-infrared mapping spectrometer (NIMS) investigation. *Journal of Geophysical Research*, *104*(E5), 11827–11852. https://doi.org/10.1029/1999JE900005

Müller, U., Bubel, T., & Schulz, G. (1993). Electron impact dissociation of O: Emission cross sections for OH*, OH^{+*}, H*, and H_2O^{+*} fragments. *Zeitschrift fur Physik D Atoms Molecules Clusters*, *25*(2), 167–174. https://doi.org/10.1007/BF01450171

Nimmo, F., & Giese, B. (2005). Thermal and topographic tests of Europa chaos formation models from Galileo E15 observations. *Icarus*, *177*(2), 327–340. https://doi.org/10.1016/j.icarus.2004.10.034

Nimmo, F., & Manga, M. (2002). Causes, characteristics and consequences of convective diapirism on Europa. *Geophysical Research Letters*, *29*(23). https://doi.org/10.1029/2002GL015754

Nimmo, F., & Manga, M. (2009). Geodynamics of Europa's icy shell. In R. T. Pappalardo, W. B. McKinnon, & K. K. Khurana (Eds.), *Europa* (pp. 381–404).

Ojakangas, G. W., & Stevenson, D. J. (1989). Thermal state of an ice shell on Europa. *Icarus*, *81*(2), 220–241. https://doi.org/10.1016/0019-1035(89)90052-3

Paganini, L., Villanueva, G. L., Roth, L., Mandell, A. M., Hurford, T. A., Retherford, K. D., & Mumma, M. J. (2019). A measurement of water vapour amid a largely quiescent environment on Europa. *Nature Astronomy*, *4*, 266–272. https://doi.org/10.1038/s41550-019-0933-6

Pappalardo, R. T. (2010). Seeking Europa's Ocean. In C. Barbieri, S. Chakrabarti, M. Coradini, & M. Lazzarin (Eds.), *Galileo's medicean moons: Their impact on 400 years of discovery* (Vol. 269, pp. 101–114). https://doi.org/10.1017/S1743921310007325

Pappalardo, R. T., Belton, M. J. S., Breneman, H. H., Carr, M. H., Chapman, C. R., Collins, G. C., et al. (1999). Does Europa have a subsurface ocean? Evaluation of the geological evidence. *Journal of Geophysical Research*, *104*(E10), 24015–24055. https://doi.org/10.1029/1998JE000628

Phillips, C. B., McEwen, A. S., Hoppa, G. V., Fagents, S. A., Greeley, R., Klemaszewski, J. E., et al. (2000). The search for current geologic activity on Europa. *Journal of Geophysical Research*, *105*(E9), 22579–22598. https://doi.org/10.1029/1999JE001139

Phillips, C. B., & Pappalardo, R. T. (2014). Europa clipper mission concept: Exploring Jupiter's ocean moon. *Eos, Transactions American Geophysical Union*, *95*(20), 165–167. https://doi.org/10.1002/2014EO200002

Quick, L. C., & Marsh, B. D. (2016). Heat transfer of ascending cryomagma on Europa. *Journal of Volcanology and Geothermal Research*, *319*, 66–77. https://doi.org/10.1016/j.jvolgeores.2016.03.018

Rathbun, J. A., Musser, J., George, S., & Squyres, S. W. (1998). Ice diapirs on Europa: Implications for liquid water. *Geophysical Research Letters*, *25*(22), 4157–4160. https://doi.org/10.1029/1998GL900135

Reynolds, R. T., Squyres, S. W., Colburn, D. S., & McKay, C. P. (1983). On the habitability of Europa. *Icarus*, *56*(2), 246–254. https://doi.org/10.1016/0019-1035(83)90037-4

Rhoden, A. R., Hurford, T. A., Roth, L., & Retherford, K. (2015). Linking Europa's plume activity to tides, tectonics, and liquid water. *Icarus*, *253*, 169–178. https://doi.org/10.1016/j.icarus.2015.02.023

Roth, L., Retherford, K. D., Ivchenko, N., Schlatter, N., Strobel, D. F., Becker, T. M., & Grava, C. (2017). Detection of a hydrogen corona in HST Lyα Images of Europa in transit of Jupiter. *The Astronomical Journal*, *153*(2), 67. https://doi.org/10.3847/1538-3881/153/2/67

Roth, L., Retherford, K. D., Saur, J., Strobel, D. F., Feldman, P. D., McGrath, M. A., & Nimmo, F. (2014). Orbital apocenter is not a sufficient condition for HST/STIS detection of Europa's water vapor aurora. *Proceedings of the National Academy of Sciences*, *111*(48), E5123–E5132. https://doi.org/10.1073/pnas.1416671111

Roth, L., Saur, J., Retherford, K. D., Strobel, D. F., Feldman, P. D., McGrath, M. A., & Nimmo, F. (2014). Transient water vapor at Europa's South Pole. *Science*, *343*(6167), 171–174. https://doi.org/10.1126/science.1247051

Rountree, S. P., & Henry, R. J. (1972). Electron-impact excitation cross sections for atomic oxygen: 3P-3s $^3S^0$. *Physical Review A*, *6*(6), 2106–2109. https://doi.org/10.1103/PhysRevA.6.2106

Rubin, M., Jia, X., Altwegg, K., Combi, M. R., Daldorff, L. K. S., Gombosi, T. I., et al. (2015). Self-consistent multifluid mhd simulations of europa's exospheric interaction with jupiter's magnetosphere. *Journal of Geophysical Research: Space Physics*, *120*(5), 3503–3524. https://doi.org/10.1002/2015ja021149

Rugamas, F., Roundy, D., Mikaelian, G., Vitug, G., Rudner, M., Shih, J., et al. (2000). Angular profiles of molecular beams from effusive tube sources: I. Experiment. *Measurement Science and Technology*, *11*(12), 1750–1765. https://doi.org/10.1088/0957-0233/11/12/315

Saur, J., Feldman, P. D., Roth, L., Nimmo, F., Strobel, D. F., Retherford, K. D., et al. (2011). HST/ACS observations of Europa's atmospheric UV emission at eastern elongation. *The Astrophysical Journal*, *738*(2), 153–165. https://doi.org/10.1088/0004-637X/738/2/153
Schmidt, J., Brilliantov, N., Spahn, F., & Kempf, S. (2008). Slow dust in Enceladus' plume from condensation and wall collisions in tiger stripe fractures. *Nature*, *451*(7179), 685–688. https://doi.org/10.1038/nature06491
Sparks, W. B., Hand, K. P., McGrath, M. A., Bergeron, E., Cracraft, M., & Deustua, S. E. (2016). Probing for evidence of plumes on Europa with HST/STIS. *The Astrophysical Journal*, *829*(2), 121. https://doi.org/10.3847/0004-637X/829/2/121
Sparks, W. B., Schmidt, B. E., McGrath, M. A., Hand, K. P., Spencer, J. R., Cracraft, M., & E Deustua, S. (2017). Active Cryovolcanism on Europa? *The Astrophysical Journal Letters*, *839*(2), L18. https://doi.org/10.3847/2041-8213/aa67f8
Squyres, S. W., Reynolds, R. T., & Cassen, P. M. (1983). Liquid water and active resurfacing on Europa. *Nature*, *301*(5897), 225–226. https://doi.org/10.1038/301225a0
Thompson, P. A., & Sonin, A. A. (1973). Compressible-fluid dynamics. *Physics Today*, *26*(3), 65–69. https://doi.org/10.1063/1.3127987
Thomson, R. E., & Delaney, J. R. (2001). Evidence for a weakly stratified europan ocean sustained by seafloor heat flux. *Journal of Geophysical Research*, *106*(E6), 12355–12365. https://doi.org/10.1029/2000JE001332
Vorburger, A. (2021). *Europa plumes*. Retrieved from https://osf.io/kubz7/OSF
Vorburger, A., Pfleger, M., Lindkvist, J., Holmström, M., Lammer, H., Lichtenegger, H. I. M., et al. (2019). Three-dimensional modeling of Callisto's surface sputtered exosphere environment. *Journal of Geophysical Research: Space Physics*, *124*(8), 7157–7169. https://doi.org/10.1029/2019JA026610
Vorburger, A., & Wurz, P. (2018). Europa's ice-related atmosphere: The sputter contribution. *Icarus*, *311*, 135–145. https://doi.org/10.1016/j.icarus.2018.03.022
Vorburger, A., Wurz, P., Lammer, H., Barabash, S., & Mousis, O. (2015). Monte-Carlo simulation of Callisto's exosphere. *Icarus*, *262*, 14–29. https://doi.org/10.1016/j.icarus.2015.07.035
Waite, J. H., Brockwell, T., Glein, C., Perryman, R., Bolton, S., McGrath, M., et al. (2019). MASPEX-Europa aboard Clipper: A mass spectrometer for investigating the habitability of Europa. In *Epsc-dps joint meeting 2019* (Vol. 2019).
Wilson, L., Head, J. W., & Pappalardo, R. T. (1997). Eruption of lava flows on Europa: Theory and application to Thrace Macula. *Journal of Geophysical Research*, *102*(E4), 9263–9272. https://doi.org/10.1029/97JE00412
Wurz, P., & Lammer, H. (2003). Monte-Carlo simulation of Mercury's exosphere. *Icarus*, *164*, 1–13. https://doi.org/10.1016/S0019-1035(03)00123-4
Yeoh, S. K., Chapman, T. A., Goldstein, D. B., Varghese, P. L., & Trafton, L. M. (2015). On understanding the physics of the Enceladus south polar plume via numerical simulation. *Icarus*, *253*, 205–222. https://doi.org/10.1016/j.icarus.2015.02.020
Yeoh, S. K., Li, Z., Goldstein, D. B., Varghese, P. L., Levin, D. A., & Trafton, L. M. (2017). Constraining the Enceladus plume using numerical simulation and Cassini data. *Icarus*, *281*, 357–378. https://doi.org/10.1016/j.icarus.2016.08.028
Zatsarinny, O., & Tayal, S. S. (2002). R-matrix calculation with non-orthogonal orbitals for electron-impact excitation of atomic oxygen. *Journal of Physics B: Atomic and Molecular Physics*, *35*(2), 241–253. https://doi.org/10.1088/0953-4075/35/2/304
Zolotov, M. Y., & Kargel, J. S. (2009). On the chemical composition of Europa's icy shell, ocean, and underlying rocks. In R. T. Pappalardo, W. B. McKinnon, & K. K. Khurana (Eds.). University of Arizona Press.

Erratum

In the originally published version of this article, several citations pointed to an incorrect reference. The citations have been updated and this version may be considered the authoritative version of record.